Journal of Magnetic Resonance 252 (2015) 151–162

Contents lists available at ScienceDirect

Journal of Magnetic Resonance

journal homepage: www.elsevier.com/locate/jmr

Theoretical and experimental study of ON-Resonance Saturation, an MRI sequence for positive contrast with superparamagnetic nanoparticles

S. Delangre [a], Q.L. Vuong [a], D. Henrard [a], J. Magat [b], C. Po [b], B. Gallez [b], Y. Gossuin [a,*]

[a] Biomedical Physics Department, University of Mons, 24, Avenue du Champ de Mars, 7000 Mons, Belgium
[b] Biomedical Magnetic Resonance Research Group, Louvain Drug Research Institute, Université Catholique de Louvain, 73, Avenue E. Mounier, 1200 Brussels, Belgium

ARTICLE INFO

Article history:
Received 7 August 2014
Revised 13 January 2015
Available online 27 January 2015

Keywords:
Magnetic resonance imaging
Positive contrast imaging
Off-resonance imaging
Iron oxide nanoparticles
Superparamagnetic nanoparticles
Contrast agents

ABSTRACT

Superparamagnetic iron oxide nanoparticles (SPM particles) are widely used in MRI as negative contrast agents. Their detection is sometimes difficult because negative contrast can be caused by different artifacts. To overcome this problem, MRI protocols achieving positive contrast specific to SPM particles were developed such as the ON-Resonance Saturation (ONRS) sequence. The aim of the present work is to achieve a bottom-up study of the ONRS sequence by an understanding of the physical mechanisms leading to positive contrast. A complete theoretical modeling, a novel numerical simulation approach and experiments on agarose gel phantoms on a 11.7 T MRI system were carried out for this purpose. The influence of the particle properties and concentration – as well as the effect of the sequence parameters on the contrast – were investigated. It was observed that theory and experiments were in strong agreement. The tools developed in this work allowed to predict the parameters leading to the maximum contrast. For example, particles presenting a low transverse relaxivity can provide an interesting positive contrast after optimization of their concentration in the sample.

1. Introduction

Magnetic Resonance Imaging (MRI) is a non-invasive biomedical imaging technique which provides images with an excellent intrinsic contrast [1]. However, the use of contrast agents is sometimes necessary to highlight specific regions such as tumors. Superparamagnetic iron oxide nanoparticles (SPM particles) are biocompatible and non-toxic contrast agents that drastically decrease the transverse relaxation times T_2 and T_2^* in their surroundings, and are thus used as negative contrast agents in T_2 or T_2^*-weighted images [2,3].

In the last decade, many studies were devoted to the optimization of the synthesis and the tuning of the SPM particle properties for MRI applications [4–10]. Nowadays, SPM particles are used in the development of cellular imaging [11–13], drug delivered therapy [14,15], hyperthermia [16], to detect arthrosclerosis plaques [17,18] or to target tumors [19,20].

The detection of SPM particles with T_2^*-weighted MRI sequences can be challenging because hypointense signals can be created by other sources such as air bubbles, calcification or interfaces between tissues. Moreover, the detection of particles can also be difficult in areas presenting low signal.

To overcome these problems, new imaging sequences leading to positive contrast with SPM particles have been developed [21–24]: the 'Off-Resonance Imaging' [25–27], the 'Off-Resonance Saturation' [28–30], the 'white-marker method' [31–33] and other techniques using post-processing image analysis [34,35] and susceptibility weighted images [36]. All these techniques take advantage of the dipolar magnetic field created by the SPM particles, which induces a water proton resonance frequency shift in the SPM particle surroundings. A comparison of these sequences are made in [37].

Finally, the ON-Resonance Saturation method (ONRS) has been developed by Stuber et al. [38], and tested in vivo in [39–42]. This sequence uses a saturation pulse to destroy the signal created by the on-resonance water protons, situated far from the SPM particles. The water protons near the SPM particles – undergoing a frequency shift – are not affected by this saturation pulse, which leads to positive contrast in the following imaging sequence.

Even if an empirical description of the ONRS contrast has been developed by Farrar et al. [43], no theoretical study has been carried out to fully understand the physical mechanisms leading to positive contrast. The lack of such study complicates the optimization of the ONRS sequence parameters and SPM particles.

This work provides a new numerical simulation approach and a theoretical modeling of the contrast generated by the ONRS sequence. This theoretical model, valid for all types of SPM particles, is developed from microscopic considerations and does not

* Corresponding author.
E-mail address: yves.gossuin@umons.ac.be (Y. Gossuin).

http://dx.doi.org/10.1016/j.jmr.2015.01.007
1090-7807/

depend on any empirical considerations. MR experiments on agarose gel phantoms on a 11.7 T system were carried out to confront the theoretical and the simulation predictions to experimental results. The dependence of the ONRS contrast on the SPM particle concentration, the ON-Resonance Saturation bandwidth, the echo time and the SPM particle properties was investigated.

2. Theory

The theory developed in this work to describe the ONRS sequence uses a bottom-up approach, starting from very fundamental theoretical derivations and finally providing an analytical expression of the contrast. The magnetic field produced by the SPM particles is first described and an analytical expression of the amount of unsaturated protons by the saturation pulse is given. The dependence of the contrast on the sequence parameters and particle properties is eventually obtained.

2.1. ONRS sequence

At high magnetic field, SPM particles can be modeled by a magnetic dipole aligned with the main magnetic field $\vec{B}_0$ (conventionally aligned with the z-axis). The magnitude of the magnetic dipole is proportional to B_{eq}, the equatorial field of the particle defined as the field created by the SPM particle at its equator. It is proportional to the SPM particle magnetization M_S (expressed in Am^2/kg [Fe]) and for magnetite it is given by (see Section 1 of the supplementary material and Ref. [4])

$$B_{eq} = 0.72 \cdot 5185 \cdot \frac{\mu_0}{3} M_S, \tag{1}$$

where 0.72 is the fraction of iron in magnetite, 5185 is the magnetite density (kg/m^3) and μ_0 is the magnetic permeability of vacuum. A SPM particle produces a dipolar magnetic field (Fig. 1) whose longitudinal component (aligned with $\vec{B}_0$) is given by

$$\vec{B}_{dip}(\vec{r}) = \frac{B_{eq} R_p^3}{r^3}(3\cos^2\theta - 1)\vec{1}_z, \tag{2}$$

where $\vec{r}$ is the vector connecting the center of the SPM particle to the considered position, θ is the angle between $\vec{r}$ and $\vec{B}_0$, and R_p is the SPM particle radius. This dipolar magnetic field implies an angular frequency shift of the water protons located at this considered position given by

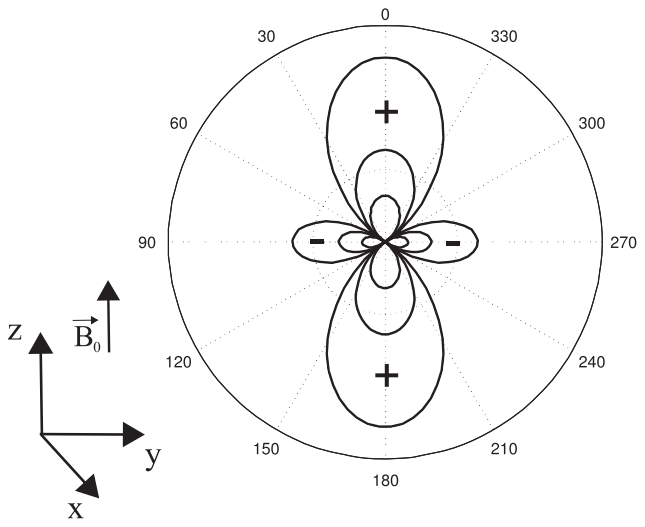

Fig. 1. Isofield lines of the dipolar magnetic field created by a SPM particles.

$$\omega_{dip}(\vec{r}) = \gamma B_{dip}(\vec{r}) \tag{3}$$

where γ is the proton gyromagnetic ratio. This frequency shift induces a frequency distribution broadening in a solution containing SPM particles (Fig. 2a).

The ONRS sequence principle is to apply a specific ON-Resonance Saturation pulse before the imaging sequence acquisition [38] (Fig. 2). As shown in Fig. 2b, this saturation pulse is tuned to spoil (saturate) only the water protons undergoing an absolute frequency shift smaller than half of the saturation pulse bandwidth $\Delta\omega$ (the on-resonance protons). Eqs. (2) and (3) show that the unspoiled (unsaturated) water protons are located near the SPM particles (Fig. 2c). Therefore, the MRI signal only originates from protons near SPM particles, which leads to a positive contrast in areas containing SPM particles (Fig. 2c).

2.2. Fraction of protons unsaturated by the saturation pulse

The contrast must be proportional to the fraction of water protons unsaturated by the saturation pulse, called ψ. An analytical expression of ψ is obtained by integrating the field distribution created by SPM particles, already calculated by Brown [44], inside the range of the saturation pulse bandwidth (see Section 2 of the supplementary materials). For a solution of SPM particles presenting an equatorial field B_{eq} (expressed in tesla) and an iron concentration Cc (expressed in mM of iron), the fraction of protons unsaturated by a saturation pulse of bandwidth $\Delta\omega$ (express in hertz) is given by:

$$\psi(Cc, B_{eq}, \Delta\omega) = 1 - \frac{2}{\pi}\tan^{-1}\left(\frac{3\sqrt{3}\cdot\Delta\omega}{Cc\cdot B_{eq}}\frac{67\cdot 10^3}{4\pi\cdot 42\cdot 10^6}\right) \tag{4}$$

This function, plotted on Fig. 3a, is linear with the iron concentration for small concentrations, when the areas of unsaturated water protons near particles are not superimposed on each other (Fig. 3b). When the iron concentration is high enough, the areas of unsaturated protons near the SPM particles are superimposed (Fig. 3c) and the fraction of unsaturated protons tends to saturate to the unit.

Fig. 3a also shows that ψ is lower for high $\Delta\omega$ values. Fig. 2b shows that when the saturation pulse bandwidth increases, the fraction of water protons saturated by the saturation pulse also increases and thus ψ decreases.

2.3. Analytical expression of the contrast

The sequence used in this work was composed of a ON-Resonance Saturation pulse (ONRS) followed by a Fast Imaging with Steady state Precession sequence (FISP) [45–51], which will be called ONRS-FISP in this article (Fig. 4). A saturation pulse of 90° was assumed, which corresponds to a complete destruction of the transverse magnetization. The longitudinal relaxation between the saturation pulse and the imaging sequence was neglected, which is justified by the long T_1 values of our samples. The imaging sequence parameters are the repetition time TR, the echo time TE, the flip angle α of the excitation pulse, and the saturation pulse bandwidth $\Delta\omega$.

In the present FISP sequence, all the gradients were balanced (Fig. 4). The same flip angle was used at each excitation pulse, without alternating phase. Therefore, the effect of each imaging gradient on the protons magnetic moment between each pulse is zero. No $\alpha/2$ pre-pulse was used before the main pulse train.

The 90° saturation pulse was followed by a 5 ms spoiler gradient destroying all the transverse magnetization. Such a saturation module could be inefficient for long T_2^*. However, as the longer T_2^*

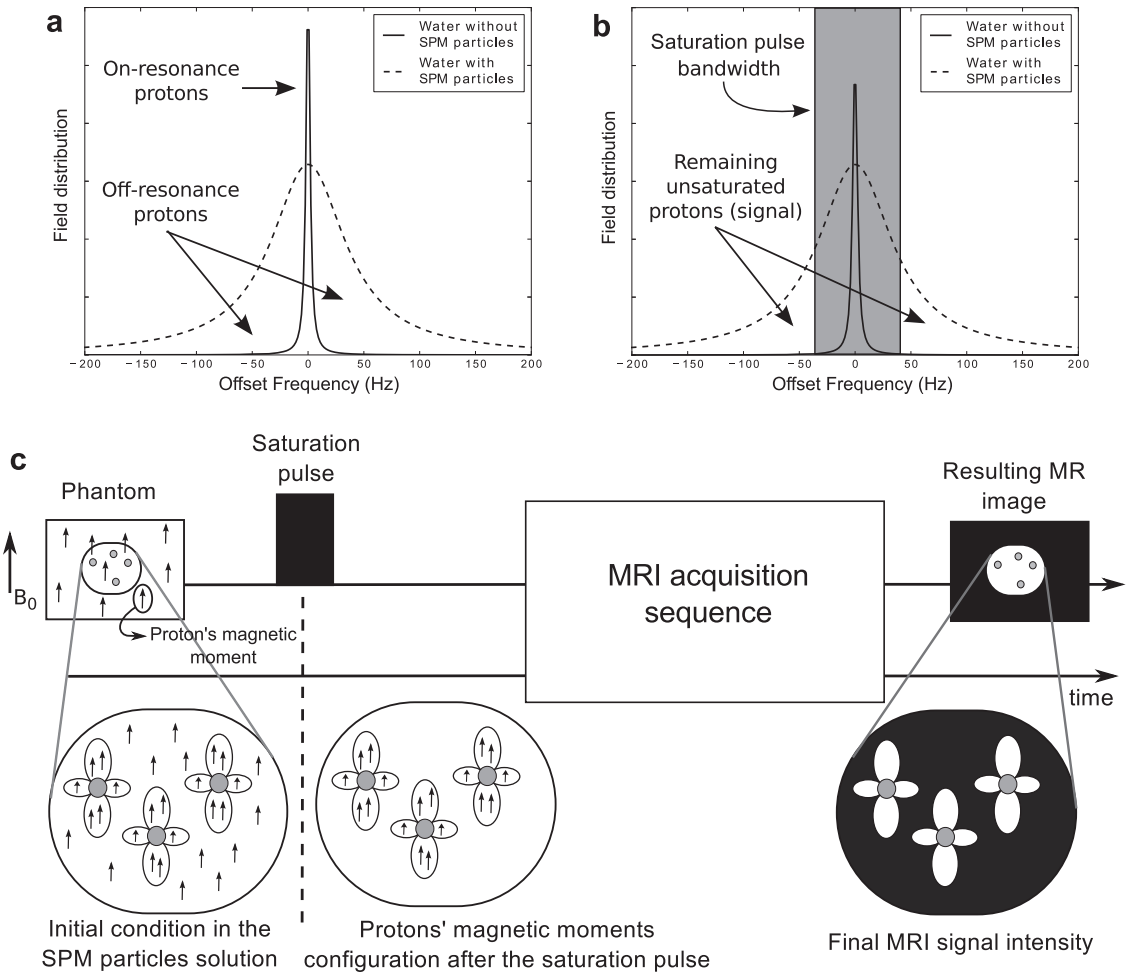

Fig. 2. ONRS concept. (a) Schematic field distribution of a solution with and without SPM particles. Due to their dipolar magnetic field, SPM particles induce a broadening of the Larmor frequency distribution. (b) The saturation pulse applied before the MRI acquisition sequence (c) saturates the on-resonance protons. The dipole geometry implies that the unsaturated protons are situated near the SPM particles, which creates positive contrast (c). (c) Representation of the ONRS sequence and the saturation pulse effect on the water proton magnetic moments.

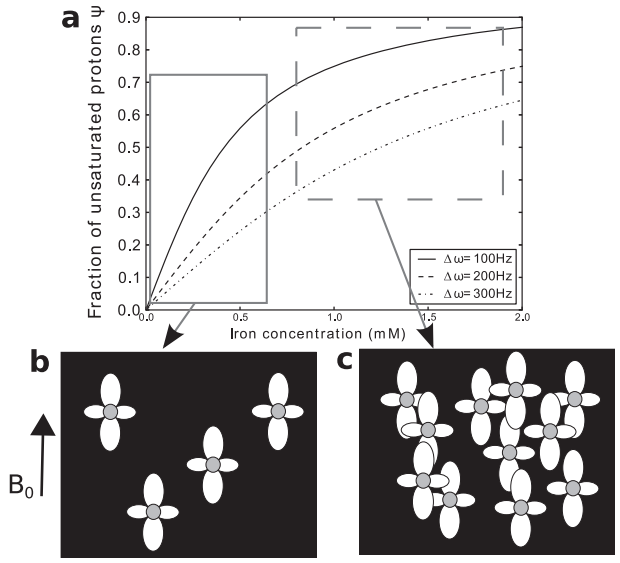

Fig. 3. Fraction water protons unaffected by the saturation pulse ψ in function of iron concentration for different values of $\Delta\omega$. (a) ψ increases linearly with iron concentration when the regions of unsaturated protons (white) are not superimposed (b). (c) ψ reaches a maximum value when these regions are superimposed.

of our phantom was 80 ms (for pure agarose gel), we can suppose that this saturation pulse is effective for our experiments.

To model the contrast created by ONRS, let us consider a solution characterized by T_1 and T_2^* relaxation times. The global magnetization coming from the water protons of this solution after the nth excitation pulse is given by [46]

$$M^n = R_x(\alpha)M^n_-, \tag{5}$$

where M^n_- is the magnetization before the n^{th} excitation pulse and $R_x(\alpha)$ is the rotation matrix around the x-axis, corresponding to the excitation pulse with an angle α:

$$R_x(\alpha) = \begin{pmatrix} 1 & 0 & 0 \\ 0 & \cos\alpha & \sin\alpha \\ 0 & -\sin\alpha & \cos\alpha \end{pmatrix} \tag{6}$$

The MRI signal after the n^{th} pulse at the echo time TE is given by the multiplication of the transverse relaxation by the transverse magnetization $M^n_\perp$:

$$S^n = M^n_\perp e^{-TE/T_2^*}, M^n_\perp = \sqrt{(M^n_x)^2 + (M^n_y)^2} \tag{7}$$

It is important to note that T_2^* must be used in Eqs. (6) and (7) because a gradient echo sequence is used to measure the transverse MRI signal after each excitation pulse.

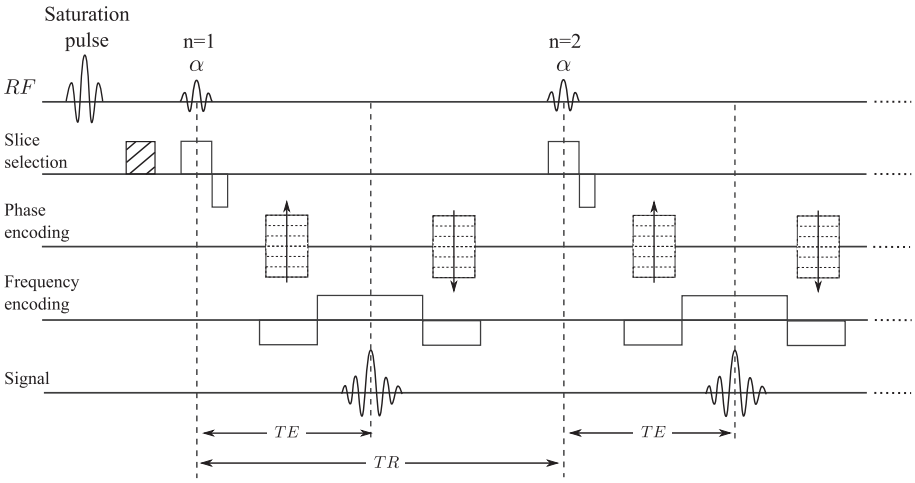

Fig. 4. The ONRS-FISP sequence. An ON-Resonance Saturation pulse, only effective at certain frequencies (see Fig. 1), is applied before the imaging sequence (FISP).

As shown in Eq. (5), the magnetization M^n can vary with the pulse number n. This is not problematic since contrast is confined in the middle of the k-space ($k_x = k_y \approx 0$). The larger values of $k_{x,y}$ are devoted to the spatial resolution. In this study, k-space is acquired starting at $k_y = 0$ and then increasing to larger values of k_y. The contrast of the experimental MRI image is thus proportional to the signal obtained after the first excitation pulse ($n = 1$). Therefore, the theory was developed with $n = 1$ to be compared to the experimental data. However, the contrast value for all n, given in Section 3 of the supplementary material, can be useful for applications using another k-space acquisition scheme or when some dummy echoes are used before the signal acquisition.

To compute the contrast, let us consider a solution characterized by the original "diamagnetic" relaxation rates $R_1 = 1/T_1$ (s^{-1}) and $R_2^* = 1/T_2^*$ (s^{-1}) divided into two regions: one containing a homogeneous solution of SPM particles and one without particles. The relaxation rates of the region without SPM particles are thus R_1 and R_2^*. If the SPM particles are characterized by relaxivities r_1 and r_2^* – defined as the relaxation rates normalized by the iron concentration – the total relaxation rates of the region containing SPM particles are given by

$$\begin{aligned} R_1' &= r_1 \cdot Cc + R_1 \\ R_2^{*\prime} &= r_2^* \cdot Cc + R_2^* \end{aligned} \tag{8}$$

where Cc is the iron concentration of SPM particles contained in this region (in mM).

The MRI signal of the region without SPM particles after the first excitation pulse is null because the saturation pulse destroys the magnetization at the beginning of the sequence, which leads to

$$S_{no-SPM} = 0 \tag{9}$$

The MRI signal coming from the region containing SPM particles is more difficult to calculate. After the application of the saturation pulse, a proton fraction ψ is unsaturated while the signal coming from the other protons is destroyed by the saturation pulse. After the excitation pulse application, the signal only comes from the unsaturated protons and is thus given, using Eqs. (5) and (7), by

$$S_{SPM} = \psi (R_x(\alpha) M^0)_\perp e^{-TE\,(R_2^* + r_2^* Cc)}, \tag{10}$$

where $M^0 = (0, 0, M_z^0)$ is the equilibrium magnetization. The contrast C obtained with ONRS-FISP is equal to the difference between the signal originating from the region containing SPM particles and the signal of the region without particles:

$$C = S_{SPM} - S_{no-SPM}. \tag{11}$$

By replacing Eqs. (9) and (10) in Eq. (11), the contrast is given by

$$C = \psi \sin\alpha\, e^{-TE(R_2^* + r_2^* Cc)} M_z^0. \tag{12}$$

This last expression only depends on the SPM particle properties, the sequence parameters and the relaxation time of the solution containing the SPM particles. This theory is 'self-consistent' because it is not based on any empirical expression.

Eq. (12) shows that the contrast is proportional to the fraction of unsaturated water protons. The exponential term corresponds to the signal decay after the excitation pulse. This decay implies an exponential dependence of the contrast on r_2^* and on the echo time.

It is interesting to note that the MR image noise is not included in equation (12) because the noise is not taken into account in the theory. It is introduced through a corrective constant factor. This factor also takes into account the proton density, present in eq. (12) through M_z^0. All the theoretical predictions were indeed multiplied by this factor to fit the experimental results. Experimentally, the noise contribution is strongly dependent on the image resolution (it decreases for increasing resolution), the coil, and the MRI scanner field.

3. Materials and methods

3.1. Phantoms

The SPM particles used in this work are composed of magnetite. Two types of SPM particles were used in this study. The first particles were the VSOP particles provided by Ferropharm (Teltow, Germany), categorized as small Superparamagnetic Particles of Iron Oxide (SPIO). The 3 nm-VSOP, 10 nm-VSOP and 20 nm-VSOP, which had diameters of 3, 10 and 20 nm respectively, were used. The second type of SPM particles were Micrometer Particles of Iron Oxide (MPIO), provided by ProMag Magnetic Microspheres, Bangs Laboratories, Inc (Indiana, USA). They are constituted of SPM crystals clustered in a polymer matrix with an overall diameter of 1 μm (1 μm-MPIO) and 3 μm (3 μm-MPIO).

In this study, several phantoms were used for different purposes. First, a phantom was built to demonstrate the better discrimination of SPM particles from other sources of signal loss, such as air bubbles, when using ONRS-FISP. This phantom was composed of three tubes containing VSOP-particles dispersed in 1.5% agarose gel, one empty tube and one tube filled with 1.5% agarose gel and a piece of plastic. A smaller empty tube was

introduced into one of the tubes filled with SPM particles. All tubes were immersed in a tube of 2.7 cm diameter filled with 1.5% agarose gel.

Second, in order to characterize the influence of the ONRS-FISP sequence parameters and of the SPM particle properties on the MRI contrast, several phantoms were prepared using different types of SPM particles dispersed in 1.5% agarose gel. These phantoms were composed of five 6 mm-diameter plastic tubes containing a colloidal suspension of SPM particles. These tubes were immersed in a tube of 2.7 cm diameter filled with a 1.5% agarose gel without SPM particles.

3.2. SPM particle characterization

The iron concentration of the samples was determined by ICP-AES (Inductively Coupled Plasma-Atomic Emission Spectrometry) after microwave digestion.

The longitudinal and transverse relaxivities of the SPM particles and the relaxation times of the agarose gel were measured on a 11.7 T MRI scanner (Bruker, Biospec, Etlingen, Germany) at room temperature. The longitudinal relaxation rate was measured with an EPI-T_1 map and the transversal relaxation rate was measured with a Multi-Slice Multi Echo (MSME) sequence using an echo time of 10 ms.

The magnetometry curves were carried out with a mini high field Vibrating Sample Magnetometer (VSM) measurement system of Cryogenics (London, UK) at 298 K. These curves were fitted with a Langevin function to provide the equatorial field B_{eq} and the radius R of the iron oxide mono-crystals constituting the particles [5].

Nuclear magnetic relaxation dispersion (NMRD) profiles were recorded on a fast field cycling relaxometer (Stelar, Italy) measuring the longitudinal relaxation rate $R_1 = 1/T_1$ over a field range of 0.3 mT–0.9 T at 37 °C.

3.3. MRI experiments

MR images were performed on an 11.7 T scanner (Bruker, Biospec, Etlingen, Germany) with a quadrature volume coil (inner diameter of 40 mm). A saturation pulse of 90° followed by a 5 ms spoiler gradient was used for all the experiments. This is the optimum angle value when the longitudinal relaxation occurring between the saturation pulse and the imaging sequence is negligible, which is the case here because of the very long T_1 values of our samples at 11.7 T. When not explicitly mentioned, the sequence parameters used in this work were given by TR = 4 ms, TE = 1.5 ms, flip angle = 10°, $\Delta\omega = 200$ Hz, matrix size = 128 × 128, FOV = 30 mm, slice thickness = 2 mm, four segments and an average number of images of 30. The saturation pulse was a three lobes sinc with a 90° flip angle. The total acquisition time was around 3 min. For a comparison of the positive contrast image with a T_2-weighted image, RARE (Rapid Acquisition with Relaxation Enhancement) images were also acquired with sequence parameters of TR/TE = 1500/15 ms and a RARE factor of 4.

The results shown in graphs correspond to the Contrast to Noise Ratio (CNR) between the area of the phantom containing SPM particles and the area of the same phantom without SPM particles. CNR is defined as

$$CNR = [S(\text{with SPM part.}) - S(\text{without SPM part.})]/\sigma_{void} \quad (13)$$

where S is the signal of the considered region and σ_{void} the standard deviation of noise. Results are expressed as the CNR mean ± the standard deviation. The Region Of Interest (ROI) was placed manually in a homogeneous area. The image processing was done with ImageJ (National Institutes of Health, Bethesda, USA).

3.4. Simulations

The numerical simulation protocol developed in this work to study the ONRS-FISP sequence is based on a microscopic approach. These simulations compute the MRI contrast between the regions with and without SPM particles.

The methodology used to compute the signal arising from a solution containing SPM particles was similar to the T_2 simulations described in the literature [7,52,53]. It was composed of three steps: (1) construction of the simulation space, (2) diffusion of the water protons and application of the ONRS-FISP sequence and (3) computation of the MRI signal, provided by the time evolution of the average proton magnetic moments.

The simulation space was composed of impenetrable SPM particles characterized by a radius R_p and an equatorial field B_{eq}. A static magnetic field $\vec{B}_0$ was imposed on the system. The SPM particles were randomly distributed in a periodic cubic space. They were assumed to be fixed in space because the Stoke-Einstein relation predicts that the diffusion coefficient of SPM particles is at least 100 times smaller than the water protons diffusion coefficient. The SPM particle magnetic moment was aligned with $\vec{B}_0$ and created a dipolar magnetic field given by Eq. (2).

After the simulation space construction, water protons were randomly distributed. The magnetic moment of each proton, written as $\vec{\mu}$, was initially aligned with $\vec{B}_0$ and its magnitude was normalized to 1.

The water proton diffusion was modeled by a random walk. At each step m, the proton position $\vec{r}(t_m)$ was incremented by a randomly oriented vector $\vec{\delta}_m$:

$$\vec{r}(t_{m+1}) = \vec{r}(t_m) + \vec{\delta}_m \text{ with } |\vec{\delta}_m| = \sqrt{6D\Delta t}. \quad (14)$$

In this expression, D is the water proton diffusion coefficient and Δt is the time step. The trajectory of a proton was supposed to be independent of the trajectories of all the other protons.

The chosen time step, $\Delta t = R_p^2/6D$, corresponded to a space jump equal to the particle radius. As the magnetic inhomogeneities are very strong near the SPM particles, the time interval was divided by 64 (and thus, the space jumps were divided by 8) when the proton was at a distance from the SPM particle center shorter than $8R_p$.

At each time step Δt, the time evolution of the proton magnetic moment was computed using a combination of the Bloch equations and classical magnetism formalism

$$\begin{cases} \mu_x(t+\Delta t) = \left[\mu_x(t)\cos\theta + \mu_y(t)sin\theta\right]e^{-\Delta t R_2^*} \\ \mu_y(t+\Delta t) = \left[\mu_x(t)sin\theta - \mu_y(t)cos\theta\right]e^{-\Delta t R_2^*} \\ \mu_z(t+\Delta t) = (1-e^{-\Delta t/T_1})M_z^0 + \mu_z(t)e^{-\Delta t R_1} \end{cases} \quad (15)$$

In this last equation, $\theta = \gamma B_{tot}(t+\Delta t)\Delta t$, γ is the proton gyromagnetic ratio, $\vec{\mu}_{x,y}$ and $\vec{\mu}_z$ are the transversal and longitudinal components of the proton magnetic moment, T_1 and T_2^* are the relaxation times of the solution without SPM particles, $\vec{r}(t)$ is the proton position at time t and $\vec{B}_{tot}$ is the total magnetic field. $\vec{B}_{tot}$ is equal to the sum of $\vec{B}_0$ and the sum of the dipolar magnetic field created at the position $\vec{r}(t)$ by all the SPM particles (given by Eq. (2)):

$$\vec{B}_{tot}(\vec{r}) = \vec{B}_0 + \sum_j \vec{B}_{dip}(\vec{r}(t) - \vec{r}_{SPM,j}), \quad (16)$$

with $\vec{r}_{SPM,j}$ the position of the SPM particle j.

It is worth noting that T_1 and T_2^* of Eq. (15) are the "diamagnetic" contribution of the solvent to the relaxation. These are not

related to the relaxation induced by the particles. Indeed, the latter is due to the diffusion of protons across the dipolar field created by the SPM particles, which is simulated through this algorithm [7].

The same methodology was used to compute the signal of a solution without SPM particles, but the total magnetic field was equal to $\vec{B}_0$ only. The ONRS-FISP sequence (Fig. 4) was applied to the water proton magnetic moment by using a rotational matrix. All the applied pulses were supposed to be perfect and instantaneous. The ON-Resonance Saturation pulse was modeled by applying a rotation of 90° around the x-axis for the protons magnetic moments undergoing a frequency shift within the saturation pulse bandwidth. These magnetic moments were then defocused to spoil their MRI signal. All the excitation pulses were modeled by a simple rotation around the x-axis of an angle equal to the excitation angle α.

The diffusion of N protons was independently simulated and the time evolution of their magnetic moment was computed to obtain the global magnetization $\vec{M}(t)$. This latter is given by the average of all the individual protons magnetic moments $\vec{\mu}(t)$

$$\vec{M}(t) = \frac{1}{N}\sum_{i=1}^{N}\vec{\mu}^i(t) \tag{17}$$

To obtain the MRI signal at the echo time TE after the n^{th} excitation pulse, the transverse component of $\vec{M}(t)$ at the time $TE + (n-1)\ TR$ was computed as

$$S^n(TE+(n-1)TR) = \sqrt{M_x^2(TE+(n-1)TR)+M_y^2(TE+(n-1)TR)} \tag{18}$$

This calculation was performed for solutions with and without SPM particles to obtain the contrast after the first excitation pulse ($n = 1$) by using Eq. (11).

The general simulation parameters were:

- Temperature: 310 K (human body temperature)
- Magnetization of magnetite: 100 Am^2/kg [Fe], corresponding to $B_{eq} = 0.16$ T
- Particle radius: 10 nm
- Longitudinal and transversal relaxation time of the solution without SPM particles: $T_1 = 3$ s, $T_2^* = 80$ ms (corresponding to the relaxation times measured for a 1.5% agarose gel)
- Water proton diffusion coefficient D at 310 K : 3×10^{-9} m^2/s

These parameters led to a simulated transverse relaxivity equal to $r_2^* = 300$ mM^{-1} s^{-1} and $r_1 \approx 0$ mM^{-1} s^{-1}.

Table 1
Relaxivity, equatorial field and radius of the iron oxide crystals constituting the SPM particles.

Particles	$r_1(s^{-1}mM^{-1})$	$r_2(s^{-1}mM^{-1})$	B_{eq}(T)	R(nm)
3 nm-VSOP	2.1	90	0.13	3.74
10 nm-VSOP	2.2	170	0.12	5.7
20 nm-VSOP	2.1	240	0.13	4.21
1 μm-MPIO	~0	600	0.17	5.13
3 μm-MPIO	~0	/	0.16	5.14

The ONRS-FISP sequence parameters used in the simulations were the same as those used experimentally in order to facilitate the comparison of results. Three simulations were systematically performed for each set of parameters. The data shown in the graphs correspond to the contrast mean and the error bars represent the standard deviation calculated from these three simulations. Contrarily to the contrast to noise ratio (CNR) extracted from the experimental ONRS-FISP images, calculated with (13), the contrast computed by the simulations was defined as in Eq. (11) due to the absence of noise in the simulation protocol. Its value was comprised between 0 (no contrast) and 1 (high contrast).

The routines were written in C++, parallelized with OPNEMP and used the GNU Scientific Library. The simulations were performed with the resources of the *Consortium des Equipements de Calcul Intensif* (CECI, Université Catholique de Louvain, Université Libre de Bruxelles, Université de Liège, Université de Namur and Université de Mons). Data analysis was performed with Python, using the Numpy, Scipy and Matplotlib libraries.

4. Results

4.1. SPM particle characterization

The results (Table 1) showed a practically zero r_1 for all SPM particles and an increase of r_2 with particle size, as predicted by relaxation theories for high fields [5,7]. The relaxation time of the agarose gel was measured as $T_1 = 3$ s and $T_2 = 80$ ms. Note that the transverse relaxivity r_2 was measured with a spin echo sequence while the theory developed in this work uses the r_2^* value to predict the ONRS-FISP contrast (Eq. (12)). These values are actually equal in this work since the model developed by Gillis et al. [52] showed that $r_2 = r_2^*$ in the Motional Averaging Regime (MAR) and in the Partial Refocusing Model if $T_2 \approx TE$. The first

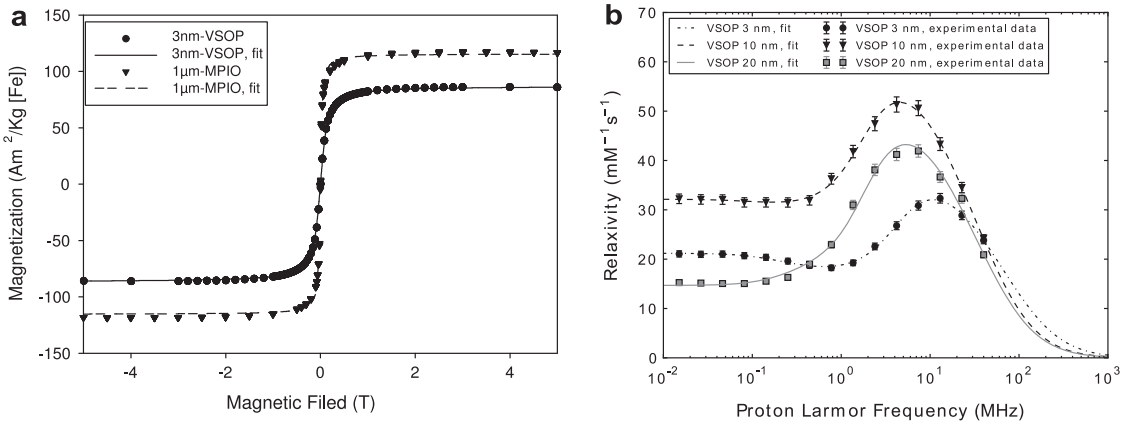

Fig. 5. SPM particle characterization. (a) Magnetometry curves of the 3 nm-VSOP and the 1 μm-MPIO, fitted with a Langevin function. (b) NMRD profile of the VSOP particles, fitted with the Roch theoretical model [54,55].

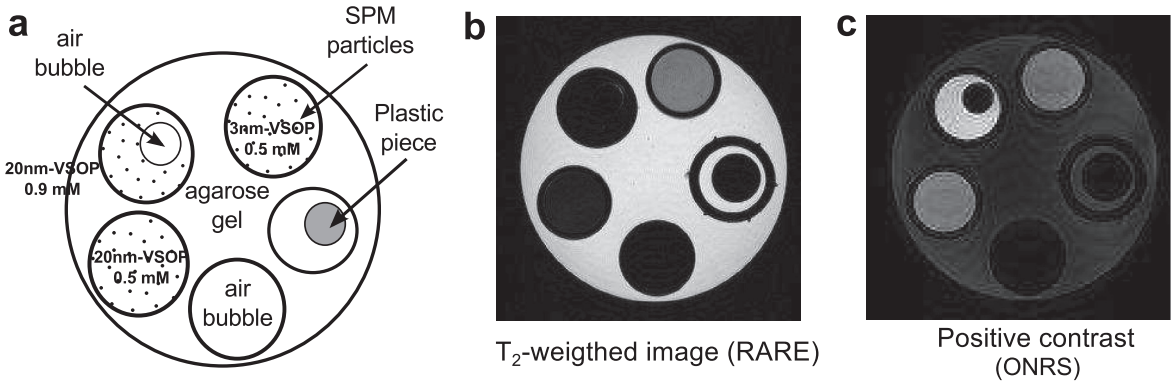

Fig. 6. MR image of a phantom created with some sources of signal loss obtained with a RARE (TR/TE = 1500/15 ms), T_2-weighted, and ONRS-FISP sequence. The RARE image shows black spots where the plastic piece, air bubbles and SPM particles are situated. SPM particles appear as bright spots on ONRS-FISP image, which makes easier their discrimination from other sources of signal loss.

condition is fulfilled for the VSOP particles while the MPIO particles meet the second one.

Magnetometry curves of 3 nm-VSOP and 1 μm-MPIO (Fig. 5b) showed the typical behavior of SPM particle suspensions [5]. The equatorial field B_{eq} and the radius R of the iron oxide crystals composing the particles are presented on Table 1. The results showed that the 10 nm-VSOP, 20 nm-VSOP, 1 μm-MPIO and the 3 μm-MPIO are constituted of a coating matrix in which crystals of magnetite with a radius of 5 nm are embedded. The 3 nm-VSOP is constituted of a single magnetite crystal.

The NMRD profile of the VSOP samples (Fig. 5b) presented the typical behavior of small SPM particles [5]. The results were fitted with the theoretical model developed by Roch et al. [54,55] (the fitting parameters are presented in Section 5 of the supplementary material). The NMRD profiles of the MPIO are not shown because the large size of these particles implies a practically zero r_1 at magnetic fields larger than 0.3 T.

4.2. Positive contrast specificity to the SPM particles

Fig. 6 shows two MR images of a phantom containing agarose gel, SPM particles, air bubbles and a plastic piece (Fig. 6a). The first one was acquired with a T_2-weighted sequence (RARE) and the second one with the ONRS-FISP sequence.

The RARE image (Fig. 6b) showed black spots for the SPM particles, the plastic piece and the air bubbles. On the contrary, the ONRS-FISP image (Fig. 6c) clearly showed a bright spot for the SPM particles while the air bubbles and the plastic piece produced negative contrast. This demonstrates the specificity of the positive contrast obtained with the ONRS-FISP sequence.

4.3. Influence of the iron concentration on the contrast

Numerical simulations and different phantoms of 20 nm-VSOP (with iron concentrations ranging from 0 mM to 0.9 mM) were

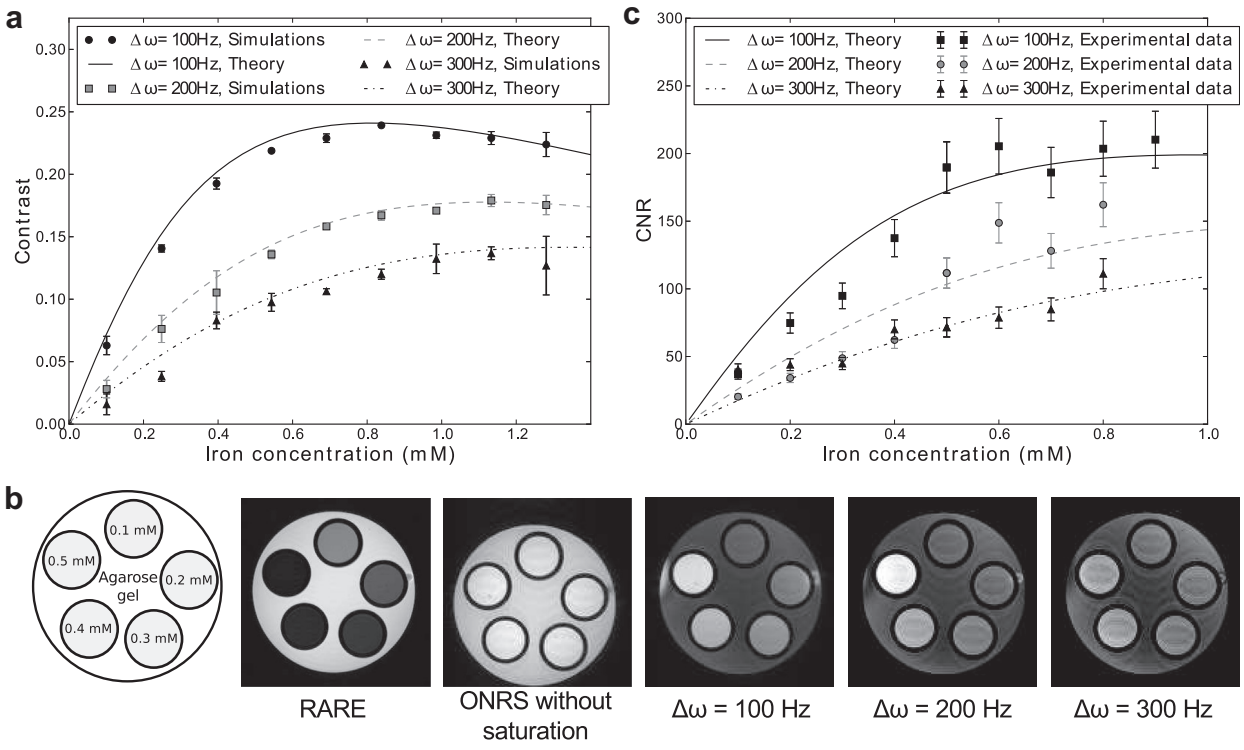

Fig. 7. Influence of iron concentration on the ONRS-FISP contrast for different values of the saturation pulse bandwidth $\Delta\omega$. (a) Numerical simulations and theory. (b) MR images of a phantom containing the 20 nm-VSOP particles obtained with ONRS-FISP, ONRS-FISP without saturation pulse and a RARE sequence (T_2 weighted). (c) Experimental data extracted from the MR images (b) and theoretical predictions (plotted via Eq. (12)).

used to study the influence of iron concentration on contrast for different values of the saturation pulse bandwidth $\Delta\omega$ (Fig. 7).

The MRI contrast calculated by the numerical simulation is shown in Fig. 7a. This graph reveals that, independently of $\Delta\omega$, the contrast increased linearly with the iron concentration until a maximum value was reached, after which it decreased. This behavior leads to an optimal concentration. The results were in accordance with the theoretical predictions, calculated with Eq. (12) using the same parameters as for the numerical simulations.

MR images of the phantoms acquired with ONRS-FISP showed positive contrast where the SPM particles were situated, with an increase of the signal intensity according to the iron concentration (Fig. 7b). Images acquired with a RARE sequence (T_2-weighted and generating negative contrast) and an ONRS-FISP sequence without the saturation pulse are also presented in Fig. 7b for comparison. The RARE image showed a decrease in the signal intensity for increasing iron concentrations and a homogeneous signal intensity appeared on the image acquired with ONRS-FISP without the saturation pulse.

The CNR estimated from the ONRS-FISP images (Fig. 7c) confirmed the theoretical and simulation results (Fig. 7a). The CNR increased with the iron concentration until a maximum value was reached. The following contrast decrease was not visible (except for 1 μm-MPIOs, whose results are presented in Fig. S3 of the supplementary materials).

Theoretical predictions plotted on Fig. 7c were obtained using Eq. (12) with the experimental parameters, such as the equatorial field and the transverse relaxivity of the SPM particles (Table 1). Even if the VSOP particles are constituted of clustered mono-crystals of magnetite, the theory shows that the mono-crystals parameters (B_{eq} and iron concentration) can be directly inserted in Eq. (12) to compute the contrast (see Section 3.4 of the supplementary material for more details). All the theoretical values were multiplied by the same corrective factor for the comparison with experimental results. This had to be done in order to take the noise into account. A strong accordance between theory and experiment is observed for the 20 nm-VSOP (Fig. 7c) and the 1 μm-MPIO (Fig. S3), which confirmed that the theory allows to estimate the contrast produced by different types of SPM particles.

The contrast dependence on the iron concentration can be interpreted thanks to the theoretical model. Eq. (12) shows that the contrast value results from the competition of two contributions: (i) the fraction of protons unaffected by the saturation pulse ψ, which increases with the particle concentration (Fig. 3 and Eq. (4)), and (ii) the signal decay due to the transverse relaxation induced by the SPM particles, included in the exponential term $e^{-r_2^* Cc\ TE}$. For small iron concentrations, the contrast dependence on the iron concentration is given by ψ because $e^{-r_2^* Cc\ TE} \approx 1$. The linearity of ψ with the iron concentration at this stage explains the linear dependence of the contrast with the concentration for small concentrations. In opposite, for high iron concentrations, the term $e^{-r_2^* Cc\ TE}$ dominates the contrast behavior, which leads to a contrast decrease with the increase of the iron concentration when the concentration is high enough.

4.4. Influence of the saturation pulse bandwidth $\Delta\omega$ on the contrast

Numerical simulations and MR images of the phantom containing different concentrations of 20 nm-VSOP were performed for different values of $\Delta\omega$ in order to examine its influence on the ONRS-FISP contrast (Fig. 7).

Numerical simulations (Fig. 7a and Fig. S5) showed that higher contrast was observed for lower values of $\Delta\omega$, independently of the iron concentration. This observation was validated by the ONRS-FISP images (Fig. 7b), where the contrast was higher for $\Delta\omega = 100$ Hz than for $\Delta\omega = 300$ Hz. The CNR extracted from the ONRS-FISP images (Fig. 7c and Fig. S6) were in agreement with the theoretical predictions and confirmed that the contrast decreased when $\Delta\omega$ increased.

Theoretically, the contrast decrease with $\Delta\omega$ can be understood by considering Eq. (12), which shows that the contrast dependence on $\Delta\omega$ is only included in ψ (it is experimentally proved in Section 4 of the supplementary materials). As the contrast is proportional to ψ and ψ decreases when $\Delta\omega$ increases (4), the contrast has to decrease when $\Delta\omega$ increases.

4.5. Influence of the echo time TE on the contrast

Numerical simulations and experiments on the agarose gel phantom containing 20 nm-VSOP in different concentrations were performed to study the influence of the echo time (TE) at different iron concentrations (Fig. 8). All the results were obtained with a repetition time TR of 10 ms.

The numerical simulations results obtained with different TE (Fig. 8a), which were in good agreement with the theoretical predictions, showed that the contrast was higher for lower values of TE. This behavior was more pronounced for large iron concentrations. The contrast dependence on the iron concentration was similar to what was described in the previous sections.

The MR images acquired with the ONRS-FISP sequence at different echo times showed a contrast decrease when TE increased (Fig. 8b). This decrease was more pronounced for high iron concentrations as expected from the previous results. The RARE image showed black spots where the SPM particles were situated and the MR image acquired with the ONRS-FISP sequence without saturation did not present any contrast.

The CNR estimated from the images acquired with ONRS-FISP (Fig. 8c) confirmed the last observations and was in accordance with the simulation results. The optimum iron concentration clearly depended on the value of TE. The theoretical predictions, computed from Eq. (12) with the experimental parameters and scaled by the same correcting factor, were in line with the experimental data. Similar results were obtained with the 1 μm-MPIO (Fig. S4).

The contrast behavior for varying echo times is theoretically explained by the exponential dependence of the contrast on the echo time (Eq. (12)) (illustrated on Fig. S7 and S8). As for all MR imaging sequences, the contrast exponentially decreased after the excitation pulse. Therefore, the measured signal, and thus the contrast, has to decrease with the increase of TE. As the iron concentration appears together with TE in the exponential argument of Eq. (12), TE had a greater influence on the contrast for high iron concentrations.

4.6. Optimal SPM particles for ONRS-FISP

A phantom containing different types of SPM particles (the 3 nm-VSOP, 10 nm-VSOP, 20 nm-VSOP, 1 μm-MPIO and 3 μm-MPIO at an iron concentration of 0.5 mM) and numerical simulations were used to study the influence of the SPM particle properties on the ONRS-FISP contrast. Eq. (12) predicts that SPM particles only influence the ONRS-FISP contrast through their equatorial field and their relaxivities.

All the SMP particles used in this work were composed of magnetite crystals, all having approximately the same equatorial field and r_1 at 11.7 T, but presenting different transverse relaxivities r_2^* (Table 1). Therefore, only the r_2^* influence on the contrast could be studied.

Numerical simulations using SPM particles possessing different r_2^* were performed to study the r_2^* influence on the contrast

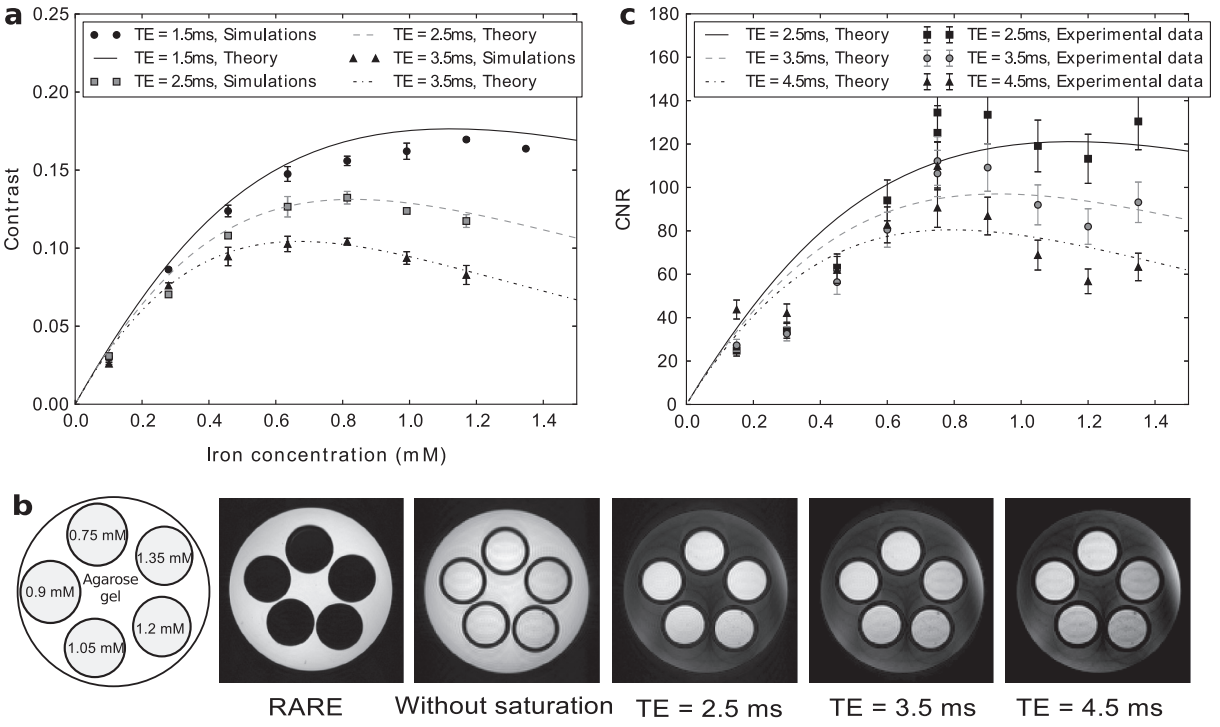

Fig. 8. Influence of the iron concentration on the ONRS-FISP contrast for different values of echo time TE. (a) Numerical simulations and theory. (b) MR image of a phantom containing 20 nm-VSOP particles in different concentration obtained with a RARE sequence (T_2-weighted), ONRS-FISP without saturation pulse and ONRS-FISP for different echo times. (c) CNR extracted from phantoms containing 20 nm-VSOP.

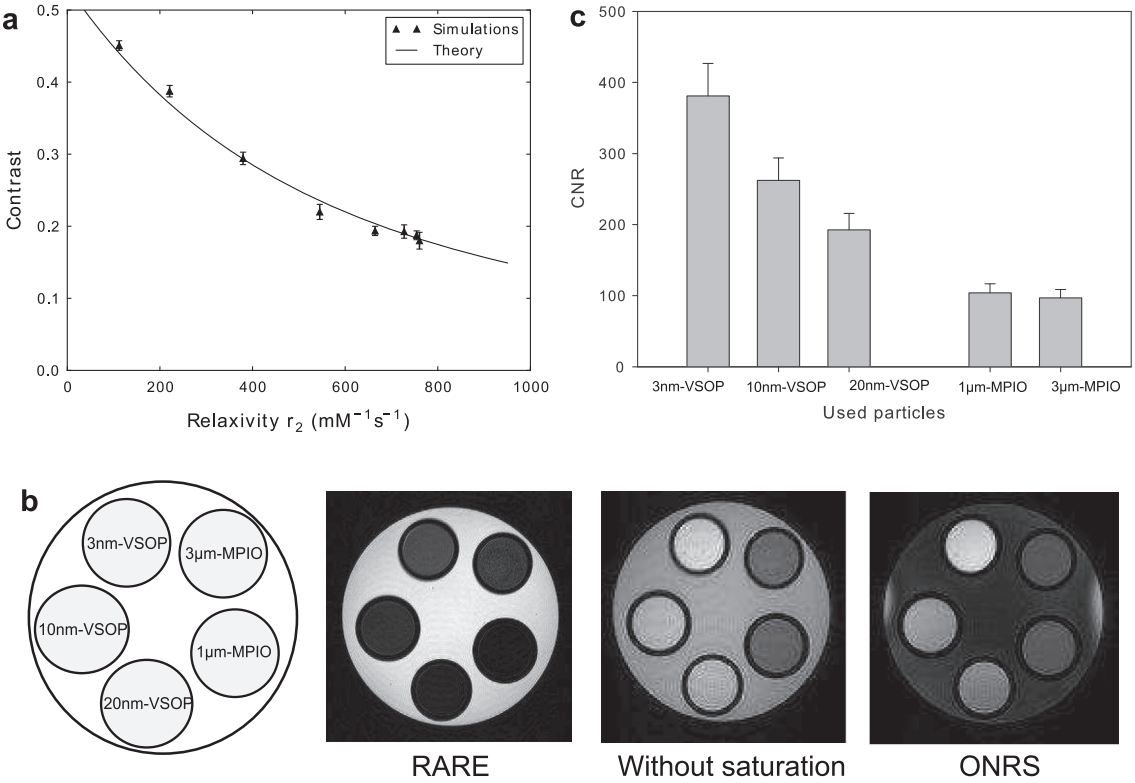

Fig. 9. SPM particle transverse relaxivity influence on the contrast. (a) Numerical simulations and theoretical predictions. (b) MR image of a phantom containing different types of particles with an iron concentration of 0.5 mM. (c) CNR measured on the MR images.

(Fig. 9a). The results were congruent with theoretical predictions: the contrast decreases exponentially when r_2^* increases.

The MR image of the phantom obtained with the ONRS-FISP sequence presented on Fig. 4 without saturation pulse showed that the signal decreased with r_2^* for the VSOP particles (Fig. 9b). The signal for MPIO particles seemed comparable for 1 μm-MPIO and 3 μm-MPIO.

The comparison between the MR images obtained with ONRS-FISP with and without the saturation pulse and the r_2^* values (Table 1) revealed that the contrast decreased when r_2^* increased, as predicted by the theory and simulations. The contrast of the two types of MPIO particles was approximately identical, probably because they present similar r_2^*. The CNR extracted from the ONRS-FISP image (Fig. 9c) confirmed this observation.

The contrast decrease observed for increasing r_2^* is explained by the theoretical model through the exponential dependence of the contrast on r_2^* in Eq. (12). The increase of r_2^* involves a faster signal decay after the last excitation pulse, leading to a decrease of the MRI signal and thus, of the ONRS-FISP contrast. SPM particles with low transverse relaxivity must therefore be preferred when using ONRS-FISP.

5. Discussion

This work presents an original approach of the ON-Resonance water Saturation sequence coupled with a FISP imaging sequence (ONRS-FISP), which provides positive contrast with SPM particles. Previous studies [38,40–43] have demonstrated the possibility to get positive contrast with ONRS in vitro and in vivo but did not provide any theoretical understanding of the contrast dependence on the sequence and the SPM particle parameters.

The aim of this work was to study the physical mechanisms leading to positive contrast. For this purpose, a new numerical simulation program was elaborated and a theoretical modeling was developed using a bottom-up approach. This model is able to predict the contrast generated by the ONRS sequence and its dependence on the sequence and the SPM particle parameters.

Experiments on agarose gel phantoms containing SPM particles were carried out in order to compare the theory and the simulations results to the experimental data. The results showed a strong accordance between theory, simulations and experiments for the different types of SPM particles used in this work. Theory and simulations are thus two important tools allowing the study of the positive contrast generated by the ONRS sequence.

Thanks to the absence of empirical assumptions, the developed simulations and theory can be adapted to study other positive contrast sequences. For example, the theory could be adapted to study the ONRS sequence combined with a Spin-Echo (SE) acquisition sequence. In this case, the contrast can be approximated by $C \propto \psi e^{-TE(r_2 Cc+R_2)}$ (see Section 7 of the supplementary material). The similarity between this expression and Eq. (12) shows that the ONRS-SE contrast behavior will be the same as for ONRS-FISP. Similarly, the theoretical model and simulations can be adapted to study the contrast created by a FISP sequence using an $\alpha/2$ prepulse and flip angles with alternating phases.

In addition, the theory could be adapted for a non-ideal saturation pulse (an ideal square saturation pulse shape was assumed in this work) by calculating the ψ function on the desired pulse shape. In this case, the frequency selection would not be as accurate as for perfect pulses. This would saturate some protons nearby the SPM particles, which would lead to a loss of contrast.

The sequence used in this study is constituted of a frequency selective ON-Resonance Saturation pulse followed by a FISP image acquisition sequence (ONRS-FISP). The main advantage of this sequence is its rapidity compared to the ONRS sequences coupled with a RARE or a SE sequence (2–3 min for ONRS-FISP, compared to 6–7 min for ONRS combined with a SE or a RARE imaging sequence).

Preliminary results show that an acceptable amount of contrast can be reached for rather low iron concentrations (~0.5 mM), similar to the in vivo iron concentration reached in organs targeted by SPM particles. The results also show a non-linear dependence of the contrast on the iron concentration for concentrations larger than a threshold value, which confirms the observations of reference [43]. An optimum iron concentration, which can be computed thanks to the theoretical model, was observed. However, in vivo, the iron concentration is almost impossible to control accurately since it depends on many parameters, which makes its optimization really difficult.

Inversely, the interest of this sequence could be precisely to measure the iron concentration in cellular or molecular imaging applications. This cannot be done with a single image but thanks to the theory, it could be possible to estimate the iron concentration by varying the sequence parameters, as $\Delta\omega$, and observe the change in contrast. The resulting curves could be fitted by the theory to obtain an estimate of the iron concentration. This method will be developed in a future work.

The decrease of the contrast with the increase of TE shows that TE must be as small as possible to maximize the contrast, as noted in [38,43]. Moreover, a long echo time produces more artefacts in the MR image, as it can be seen in the right edge of the phantom on Fig. 8b.

The contrast was also shown to be higher for low saturation pulse bandwidths $\Delta\omega$. However, $\Delta\omega$ must be large enough to spoil the background signal and to reduce the artefacts due to the field inhomogeneities, which could lead to erroneous positive contrast as seen in the left edge of the phantom presented on Fig. 7b. Therefore, the optimal value of $\Delta\omega$ is a compromise between the contrast value and the contrast specificity.

Finally, the phantom containing different types of SPM particles shows that, for the same equatorial field, SPM particles possessing a small transverse relaxivity must be preferred to optimize contrast. ONRS-FISP was finally shown to be able to generate positive contrast with different kinds of SPM particles if the parameters were well chosen.

This work focused on the theoretical prediction of the contrast generated by a homogenous solutions of SPM particles in an agarose gel matrix. In order to get closer to the in vivo applications, further work is needed to study the contrast obtained with SPM particles loaded cells. Indeed, the SPM particle internalization in cells affects the SPM particle properties [56,57] and thus, the contrast obtained with the ONRS-FISP sequence. In-vivo studies would also be necessary to improve the ONRS-FISP sequence for in vivo applications. An adaptation of the theory and the numerical simulations could be done in order to optimize the sequence parameters. This would also ease the determination of the particle concentration in vivo, which is an important feature for applications as cellular and molecular imaging. Finally, the relationship between the specificity and the sensitivity should also be investigated in vivo, as preliminary studied by Farrar et al. [43].

Unfortunately, ONRS-FISP has several limitations. Indeed, local field inhomogeneities (expected for tissue interfaces, implants and external field heterogeneities) could lead to erroneous positive contrast in area without SPM particles. However, good shimming and/or the use of an adiabatic pulse to saturate the off-resonance water protons [58] could minimize this problem. An appropriate choice of the saturation pulse bandwidth (not too small) and echo time (as small as possible) can also reduce these artefacts.

6. Conclusion

This work provided a study of the contrast generated by the ON-Resonance water Saturation sequence coupled with a FISP (ONRS-FISP). A new numerical simulation protocol and a self-consistent theoretical model were built in order to understand the mechanisms providing the positive contrast in depth. The good accordance between simulations, theory and experimental data obtained with agarose gel phantoms proves that simulations and theory could help to predict, before MRI experiments, the positive contrast obtained with the ONRS sequence. The theoretical model and the experimental results reveal that the best contrast is achieved with SPM particles possessing a low transverse relaxivity, for low value of saturation pulse bandwidth $\Delta\omega$ and echo time and for an optimal iron concentration. However, $\Delta\omega$ must be large enough to avoid erroneous positive contrast. Future studies should be devoted to positive contrast MRI of cells loaded with SPM particles and organs containing SPM particles. Such studies combined with an adaptation of the theoretical model developed in this work would make possible the determination of the particle concentration from the signal intensity of an ONRS-FISP image.

Acknowledgments

The authors would like to thank Dr. Alain Roch for helpful discussions and the Biomedical Magnetic Resonance Research Group (UCL) members for their help on the MRI scanner. S. Delangre (F.R.S.-FNRS Research Fellow) acknowledges the F.R.S.-FNRS for financial support. This research used resources from the *'Consortium des Équipements de Calcul Intensif'* (CECI); a consortium of high-performance computing centers of UCL, ULg, UMons, and UNamur funded by F.R.S.-FNRS (Belgium).

Appendix A. Supplementary material

Supplementary data associated with this article can be found, in the online version, at http://dx.doi.org/10.1016/j.jmr.2015.01.007.

References

[1] Y. Gossuin, A. Hocq, P. Gillis, Q.L. Vuong, Physics of magnetic resonance imaging: from spin to pixel, J. Phys. Appl. Phys. 43 (2010) 213001, http://dx.doi.org/10.1088/0022-3727/43/21/213001.
[2] C. Corot, P. Robert, J.-M. Idée, M. Port, Recent advances in iron oxide nanocrystal technology for medical imaging, Adv. Drug Deliv. Rev. 58 (2006) 1471–1504, http://dx.doi.org/10.1016/j.addr.2006.09.013.
[3] Y.X. Wang, S.M. Hussain, G.P. Krestin, Superparamagnetic iron oxide contrast agents: physicochemical characteristics and applications in MR imaging, Eur. Radiol. 11 (2001) 2319–2331, http://dx.doi.org/10.1007/s003300100908.
[4] Q.L. Vuong, J.-F. Berret, J. Fresnais, Y. Gossuin, O. Sandre, A universal scaling law to predict the efficiency of magnetic nanoparticles as MRI T2-contrast agents, Adv. Healthc. Mater. 1 (2012) 502–512, http://dx.doi.org/10.1002/adhm.201200078.
[5] Y. Gossuin, P. Gillis, A. Hocq, Q.L. Vuong, A. Roch, Magnetic resonance relaxation properties of superparamagnetic particles, Wiley Interdiscip. Rev. Nanomed. Nanobiotechnol. 1 (2009) 299–310.
[6] Y. Matsumoto, A. Jasanoff, T2 relaxation induced by clusters of superparamagnetic nanoparticles: Monte Carlo simulations, Magn. Reson. Imaging. 26 (2008) 994–998, http://dx.doi.org/10.1016/j.mri.2008.01.039.
[7] Q.L. Vuong, Y. Gossuin, P. Gillis, S. Delangre, New simulation approach using classical formalism to water nuclear magnetic relaxation dispersions in presence of superparamagnetic particles used as MRI contrast agents, J. Chem. Phys. 137 (2012), http://dx.doi.org/10.1063/1.4751442.
[8] C. Boyer, M.R. Whittaker, V. Bulmus, J. Liu, T.P. Davis, The design and utility of polymer-stabilized iron-oxide nanoparticles for nanomedicine applications, NPG Asia Mater. 2 (2010) 23–30, http://dx.doi.org/10.1038/asiamat.2010.6.
[9] Y. Liu, K. Yang, L. Cheng, J. Zhu, X. Ma, H. Xu, et al., PEGylated FePt@Fe_2O_3 core-shell magnetic nanoparticles: potential theranostic applications and in vivo toxicity studies, Nanomedicine Nanotechnol. Biol. Med. 9 (2013) 1077–1088, http://dx.doi.org/10.1016/j.nano.2013.02.010.
[10] D. Forge, S. Laurent, Y. Gossuin, A. Roch, L. Vander Elst, R.N. Muller, An original route to stabilize and functionalize magnetite nanoparticles for theranosis applications, J. Magn. Magn. Mater. 323 (2011) 410–415, http://dx.doi.org/10.1016/j.jmmm.2010.09.031.
[11] J. Kolosnjaj-Tabi, C. Wilhelm, O. Clément, F. Gazeau, Cell labeling with magnetic nanoparticles: opportunity for magnetic cell imaging and cell manipulation, J. Nanobiotechnology. 11 (2013) S7.
[12] E.M. Shapiro, S. Skrtic, K. Sharer, J.M. Hill, C.E. Dunbar, A.P. Koretsky, MRI detection of single particles for cellular imaging, Proc. Natl. Acad. Sci. USA 101 (2004) 10901–10906.
[13] J.W.M. Bulte, D.L. Kraitchman, Iron oxide MR contrast agents for molecular and cellular imaging, NMR Biomed. 17 (2004) 484–499, http://dx.doi.org/10.1002/nbm.924.
[14] B. Chertok, B.A. Moffat, A.E. David, F. Yu, C. Bergemann, B.D. Ross, et al., Iron oxide nanoparticles as a drug delivery vehicle for MRI monitored magnetic targeting of brain tumors, Biomaterials 29 (2008) 487–496, http://dx.doi.org/10.1016/j.biomaterials.2007.08.050.
[15] C. Sun, J.S.H. Lee, M. Zhang, Magnetic nanoparticles in MR imaging and drug delivery, Adv. Drug Deliv. Rev. 60 (2008) 1252–1265, http://dx.doi.org/10.1016/j.addr.2008.03.018.
[16] K.C. Barick, S. Singh, D. Bahadur, M.A. Lawande, D.P. Patkar, P.A. Hassan, Carboxyl decorated Fe_3O_4 nanoparticles for MRI diagnosis and localized hyperthermia, J. Colloid Interface Sci. 418 (2014) 120–125, http://dx.doi.org/10.1016/j.jcis.2013.11.076.
[17] K. Tsuchiya, N. Nitta, A. Sonoda, H. Otani, M. Takahashi, K. Murata, et al., Atherosclerotic imaging using 4 types of superparamagnetic iron oxides: new possibilities for mannan-coated particles, Eur. J. Radiol. 82 (2013) 1919–1925, http://dx.doi.org/10.1016/j.ejrad.2013.07.017.
[18] S.G. Ruehm, C. Corot, P. Vogt, S. Kolb, J.F. Debatin, Magnetic resonance imaging of atherosclerotic plaque with ultrasmall superparamagnetic particles of iron oxide in hyperlipidemic rabbits, Circulation 103 (2001) 415–422.
[19] J.-H. Park, G. von Maltzahn, L. Zhang, M.P. Schwartz, E. Ruoslahti, S.N. Bhatia, et al., Magnetic iron oxide nanoworms for tumor targeting and imaging, Adv. Mater. 20 (2008) 1630–1635, http://dx.doi.org/10.1002/adma.200800004.
[20] X.-H. Peng, X. Qian, H. Mao, A.Y. Wang, Targeted magnetic iron oxide nanoparticles for tumor imaging and therapy, Int. J. Nanomedicine. 3 (2008) 311.
[21] C. Lin, S. Cai, J. Feng, Positive contrast imaging of SPIO nanoparticles, J. Nanomater. 2012 (2012) 1–9, http://dx.doi.org/10.1155/2012/734842.
[22] W. Liu, H. Dahnke, E.K. Jordan, T. Schaeffter, J.A. Frank, In vivo MRI using positive-contrast techniques in detection of cells labeled with superparamagnetic iron oxide nanoparticles, NMR Biomed. 21 (2008) 242–250, http://dx.doi.org/10.1002/nbm.1187.
[23] M. Wolters, M. Oostendorp, B.F. Coolen, M.J. Post, J.M.H. Janssen, G.J. Strijkers, et al., Efficacy of positive contrast imaging techniques for molecular MRI of tumor angiogenesis: POSITIVE CONTRAST MOLECULAR MRI, Contrast Media Mol. Imaging. 7 (2012) 130–139, http://dx.doi.org/10.1002/cmmi.471.
[24] J. Huang, X. Zhong, L. Wang, L. Yang, H. Mao, Improving the magnetic resonance imaging contrast and detection methods with engineered magnetic nanoparticles, Theranostics 2 (2012) 86–102, http://dx.doi.org/10.7150/thno.4006.
[25] C.H. Cunningham, T. Arai, P.C. Yang, M.V. McConnell, J.M. Pauly, S.M. Conolly, Positive contrast magnetic resonance imaging of cells labeled with magnetic nanoparticles, Magn. Reson. Med. 53 (2005) 999–1005, http://dx.doi.org/10.1002/mrm.20477.
[26] W. Foltz, C. Cunningham, A. Mutsaers, S. Conolly, D. Stewart, A. Dick, Positive-contrast imaging in the rabbit hind-limb of transplanted cells bearing endocytosed superparamagnetic beads, J. Cardiovasc. Magn. Reson. 8 (2006) 817–823, http://dx.doi.org/10.1080/10976640600777819.
[27] P. Balchandani, M. Yamada, J. Pauly, P. Yang, D. Spielman, Self-refocused spatial-spectral pulse for positive contrast imaging of cells labeled with SPIO nanoparticles, Magn. Reson. Med. 62 (2009) 183–192, http://dx.doi.org/10.1002/mrm.21973.
[28] O. Zurkiya, X. Hu, Off-Resonance Saturation as a means of generating contrast with superparamagnetic nanoparticles, Magn. Reson. Med. 56 (2006) 726–732, http://dx.doi.org/10.1002/mrm.21024.
[29] P. Krämer, X. Helluy, T. Kampf, E. Lang, P.M. Jakob, Flow-enhanced Off-Resonance Saturation for remote detection of iron-based contrast agents, Magn. Reson. Med. Off. J. Soc. Magn. Reson. Med. Soc. Magn. Reson. Med. 63 (2010) 1708–1715, http://dx.doi.org/10.1002/mrm.22354.
[30] C. Khemtong, C.W. Kessinger, J. Ren, E.A. Bey, S.-G. Yang, J.S. Guthi, et al., In vivo Off-Resonance Saturation magnetic resonance imaging of v 3-targeted superparamagnetic nanoparticles, Cancer Res. 69 (2009) 1651–1658, http://dx.doi.org/10.1158/0008-5472.CAN-08-3231.
[31] K.C. Briley-Saebo, Y.S. Cho, P.X. Shaw, S.K. Ryu, V. Mani, S. Dickson, et al., Targeted iron oxide particles for in vivo magnetic resonance detection of atherosclerotic lesions with antibodies directed to oxidation-specific epitopes, J. Am. Coll. Cardiol. 57 (2011) 337–347, http://dx.doi.org/10.1016/j.jacc.2010.09.023.
[32] J.-H. Seppenwoolde, M.A. Viergever, C.J.G. Bakker, Passive tracking exploiting local signal conservation: the white marker phenomenon, Magn. Reson. Med. 50 (2003) 784–790, http://dx.doi.org/10.1002/mrm.10574.
[33] V. Mani, K.C. Briley-Saebo, V.V. Itskovich, D.D. Samber, Z.A. Fayad, Gradient echo acquisition for superparamagnetic particles with positive contrast (GRASP): sequence characterization in membrane and glass superparamagnetic iron oxide phantoms at 1.5T and 3T, Magn. Reson. Med. 55 (2006) 126–135, http://dx.doi.org/10.1002/mrm.20739.

[34] Q. Zhao, J. Langley, S. Lee, W. Liu, Positive contrast technique for the detection and quantification of superparamagnetic iron oxide nanoparticles in MRI, NMR Biomed. 24 (2011) 464–472, http://dx.doi.org/10.1002/nbm.1608.
[35] H. Zhu, K. Demachi, M. Sekino, Phase gradient imaging for positive contrast generation to superparamagnetic iron oxide nanoparticle-labeled targets in magnetic resonance imaging, Magn. Reson. Imaging. 29 (2011) 891–898, http://dx.doi.org/10.1016/j.mri.2011.04.011.
[36] F. Eibofner, G. Steidle, R. Kehlbach, R. Bantleon, F. Schick, Positive contrast imaging of iron oxide nanoparticles with susceptibility-weighted imaging, Magn. Reson. Med. 64 (2010) 1027–1038.
[37] E.-J.P.A. Vonken, M. Schär, J. Yu, C.J.G. Bakker, M. Stuber, Direct in vitro comparison of six three-dimensional positive contrast methods for susceptibility marker imaging, J. Magn. Reson. Imaging. 38 (2013) 344–357, http://dx.doi.org/10.1002/jmri.23976.
[38] M. Stuber, W.D. Gilson, M. Schär, D.A. Kedziorek, L.V. Hofmann, S. Shah, et al., Positive contrast visualization of iron oxide-labeled stem cells using inversion-recovery with ON-resonant water suppression (IRON), Magn. Reson. Med. 58 (2007) 1072–1077.
[39] N.A. Krämer, H.C.W. Donker, J. Otto, M. Hodenius, J. Sénégas, I. Slabu, et al., A concept for magnetic resonance visualization of surgical textile implants: invest, Radiol. 45 (2010) 477–483, http://dx.doi.org/10.1097/RLI.0b013e3181e53e38.
[40] G. Korosoglou, R.G. Weiss, D.A. Kedziorek, P. Walczak, W.D. Gilson, M. Schär, et al., Noninvasive detection of macrophage-rich atherosclerotic plaque in hyperlipidemic rabbits using "Positive Contrast" magnetic resonance imaging, J. Am. Coll. Cardiol. 52 (2008) 483–491, http://dx.doi.org/10.1016/j.jacc.2008.03.063.
[41] G. Korosoglou, S. Shah, E.-J. Vonken, W.D. Gilson, M. Schär, L. Tang, et al., Off-Resonance Angiography: a new method to depict vessels—phantom and rabbit studies1, Radiology 249 (2008) 501–509.
[42] G. Korosoglou, L. Tang, D. Kedziorek, K. Cosby, W.D. Gilson, E.-J. Vonken, et al., Positive contrast MR-lymphography using inversion recovery with ON-resonant water suppression (IRON), J. Magn. Reson. Imaging 27 (2008) 1175–1180, http://dx.doi.org/10.1002/jmri.21337.
[43] C.T. Farrar, G. Dai, M. Novikov, A. Rosenzweig, R. Weissleder, B.R. Rosen, et al., Impact of field strength and iron oxide nanoparticle concentration on the linearity and diagnostic accuracy of off-resonance imaging, NMR Biomed. 21 (2008) 453–463, http://dx.doi.org/10.1002/nbm.1209.
[44] R. Brown, Distribution of fields from randomly placed dipoles: free-precession signal decay as result of magnetic grains, Phys. Rev. 121 (1961) 1379–1382, http://dx.doi.org/10.1103/PhysRev. 121.1379.
[45] M.A. Bernstein, Handbook of MRI Pulse Sequences, Academic Press, Amsterdam; Boston, 2004.
[46] Z.-P. Liang, P.C. Lauterbur, Principles of Magnetic Resonance Imaging: A Signal Processing Perspective, SPIE Optical Engineering Press, IEEE Press, Bellingham, Wash, New York, 2000.
[47] A. Oppelt, R. Graumann, H. BarfuB, H. Fischer, W. Hartl, W. Schajor, FISP-a new fast MRI sequence, Electromedica. 54 (1986) 15–18.
[48] W. Hänicke, H.U. Vogel, An analytical solution for the SSFP signal in MRI, Magn. Reson. Med. Off. J. Soc. Magn. Reson. Med. Soc. Magn. Reson. Med. 49 (2003) 771–775, http://dx.doi.org/10.1002/mrm.10410.
[49] K. Scheffler, A pictorial description of steady-states in rapid magnetic resonance imaging, Concepts Magn. Reson. 11 (1999) 291–304.
[50] Y. Zur, S. Stokar, P. Bendel, An analysis of fast imaging sequences with steady-state transverse magnetization refocusing, Magn. Reson. Med. 6 (1988) 175–193, http://dx.doi.org/10.1002/mrm.1910060206.
[51] E.M. Haacke, R.W. Brown, M.R. Thompson, R. Venkatesan, Magnetic Resonance Imaging: Physical Principles and Sequence Design, first ed., Wiley-Liss, New York, 1999.
[52] P. Gillis, F. Moiny, R.A. Brooks, OnT2-shortening by strongly magnetized spheres: A partial refocusing model, Magn. Reson. Med. 47 (2002) 257–263, http://dx.doi.org/10.1002/mrm.10059.
[53] Q.L. Vuong, P. Gillis, Y. Gossuin, Monte Carlo simulation and theory of proton NMR transverse relaxation induced by aggregation of magnetic particles used as MRI contrast agents, J. Magn. Reson. 212 (2011) 139–148, http://dx.doi.org/10.1016/j.jmr.2011.06.024.
[54] A. Roch, R.N. Muller, P. Gillis, Theory of proton relaxation induced by superparamagnetic particles, J. Chem. Phys. 110 (1999) 5403, http://dx.doi.org/10.1063/1.478435.
[55] S. Laurent, D. Forge, M. Port, A. Roch, C. Robic, L. Vander Elst, et al., Magnetic iron oxide nanoparticles: synthesis, stabilization, vectorization, physicochemical characterizations, and biological applications, Chem. Rev. 108 (2008) 2064–2110, http://dx.doi.org/10.1021/cr068445e.
[56] M. Levy, C. Wilhelm, N. Luciani, V. Deveaux, F. Gendron, A. Luciani, et al., Nanomagnetism reveals the intracellular clustering of iron oxide nanoparticles in the organism, Nanoscale. 3 (2011) 4402–4410, http://dx.doi.org/10.1039/c1nr10778j.
[57] M. Lévy, F. Gazeau, J.-C. Bacri, C. Wilhelm, M. Devaud, Modeling magnetic nanoparticle dipole-dipole interactions inside living cells, Phys. Rev. B. 84 (2011), http://dx.doi.org/10.1103/PhysRevB.84.075480.
[58] S.S. Harris, H. Mao, X.P. Hu, Adiabatic pulse preparation for imaging iron oxide nanoparticles, Magn. Reson. Med. 67 (2012) 1133–1137, http://dx.doi.org/10.1002/mrm.23091.